Competitive Nucleation Mechanism for $CsPbBr_3$ Perovskite Nanoplatelets Growth

Victor M. Burlakov[1,3], Yasser Hassan[2], Mohsen Danaie[4], Henry J. Snaith[2], and Alain Goriely[3]

[1]*Linacre College, University of Oxford, Oxford, OX1 3JA, UK*

[2]*Department of Physics, University of Oxford, Clarendon Laboratory, Parks Road, Oxford OX1 3PU, UK*

[3]*Mathematical Institute, Woodstock Road, Andrew Wiles Building, University of Oxford, Oxford, OX2 6GG, UK*

[4]*Diamond Light Source Ltd., electron Physical Science Imaging Centre (ePSIC), Harwell Science & Innovation Campus, Didcot, OX11 0DE.*

Abstract

We analyse nucleation-controlled nanocrystal growth in a solution containing surface-binding molecular ligands, which can also nucleate compact layers on the crystal surfaces. We show that if the critical nucleus size for ligands is larger and the nucleation barrier is lower than those for crystal atoms, the ligands nucleate faster than the atoms on relatively wide crystal facets but much slower, if at all, on narrow facets. Such competitive nucleation of ligands and atoms results in ligands covering predominantly wider facets, thus excluding them from the growth process, and acts as a selection mechanism for the growth of crystals with narrower facets, the so-called nanoplatelets. We illustrate this mechanism by simulating the growth process of an ensemble of crystals using a kinetic Monte-Carlo technique. Our predictions are confirmed experimentally for $CsPbBr_3$ high-quality nanoplatelets grown from the solution using a three-precursors facile synthetic approach. We find that the anisotropic crystal growth resulting in nanoplatelets is controlled by two main factors: the growth temperature and the strength of surface bonding for the passivating molecular ligands. A subtle variation in the latter parameter makes the choice of surface ligands a critical component in controlling the growth process. The present study provides a theoretical framework and a set of computational tools for the design and control of nanocrystal shapes through growth, which is essential in many nano-electronic and nano-photonic applications.

Introduction

Lead halide perovskites (LHPs) display remarkable optoelectronic properties encompassing a panchromatic absorption profile, intense narrow-band luminescence, excellent ambipolar charge transport, and low non-radiative losses, all of which makes them desirable materials for light-emitting diodes (LEDs).[1-5] Based on these unique properties and a variety of simple fabrication methods, which allow for selection space in both components of the LHPs and the device architecture, research into LHPs has been pushed to the forefront of optoelectronics community in recent years.[6, 7] Despite significant success in fabricating LHP thin films for green[8, 9], red[10-12], and near infrared[13, 14] emission LEDs, obtaining suitable structures for stable blue LHP-based emitter remains an issue.[15] The poor performance of LHP in the blue spectral range requires further understanding of their growth process and of how they can be tailored in low dimensional shapes with wide bang-gaps.

One of the approaches to synthesising LHPs highly emissive in the effective blue region (i.e. near 2.65 eV) is to create anisotropic quasi-two-dimensional $CsPbBr_3$ particles in the shape of nanoplatelets (NPLs), which produce narrow PL due to strong quantum confinement.[15-23] An efficient way of producing such nanocrystals is by using surfactants, or surface-binding molecular ligands.[24-29] For instance, synthesis of the anisotropic $CsPbBr_3$ NPLs has been established using the standard hot-injection method developed by Protesescu *et al.*[30] Initially this method has been used for producing green-emitting cubic $CsPbBr_3$ nanocrystals by appropriate choice of the concentration and type of molecular ligands in solution.[18, 19, 31-35] In the past few years the approach has been successfully implemented for solution-growth of $CsPbBr_3$ NPLs[18, 19, 22, 33, 36-41], a promising material for optoelectronic applications.[2, 42-44] Despite the clear potential of the approach its original implementation is not free of some drawbacks, e.g. the reported NPLs tendency to blend and, after a while usually lose their blue

emission .[18, 19, 31-35] The approach also has the limitation of using lead halide (PbX_2) as the only source of anion and cation in a swift metathesis reaction, which causes difficulty in tuning the composition of the nanocrystals.[41] Specifically, the presence of an excess of PbX in the reaction products along with the nanoparticles causes phase transformation of the $CsPbBr_3$ into undesired Cs_4PbBr_6.[41, 45]

Quasi-two-dimensional semiconductor quantum dots in the shape of NPLs, such as CdSe, have been the most studied[46,47], and their growth has been explained in terms of intrinsic growth instability leading to NPLs formation.[48] Such a mechanism is apparently not applicable to perovskite crystals, which in most cases grow as cuboids and only in special conditions they form NPLs. Despite experimental success in determining conditions for perovskite NPLs growth[18, 19, 33, 34, 49], little is understood about the mechanisms that lead to highly anisotropic crystal shapes and how these shapes can be designed and controlled precisely at the atomic-scale thickness. For example, Pan *et al.* [24] and other groups[18, 19, 22, 32, 36-41] report that the precise type of surface capping ligands and the reaction temperature are essential for the growth of 2D $CsPbBr_3$ perovskite NPLs. However, the physical mechanism that reveals the effect of these parameters on nanocrystal growth remains elusive.

Here, we present a model of nanocrystal growth that explains NPLs formation in terms of competitive nucleation of crystal monolayer versus ligand monolayer. Our model predicts the effects of the temperature T and ligand-ligand interaction energy ε_{LL} on the shape of growing nanocrystals. In particular, we predict that increasing ε_{LL} or decreasing T from some optimum values results in the predominant growth of thinner NPLs while changing these parameters otherwise stimulates the growth of cuboid-shaped crystals. Our experimental studies fully recover these trends and illustrate that an appropriate choice of the surface binding ligands and growth temperature result in the desired NPLs for an effective blue emission.

To validate the proposed model experimentally, we implement a new synthetic approach that allows stoichiometric control of the concentration of all elements in the reaction in contrast to the previously reported approach (i.e. Protesescu *et al.*[30] method) where PbX_2 is the only source of both anions and cations. Our synthesis is based on the three-precursor approach first reported by Wei e*t al.*[50] and adopted by others[51, 52], which initially used to synthesise $CsPbX_3$ and $FAPbX_3$ cubic nanocrystals (for more details see experimental section). We modified this approach as described below to achieve controlled growth of $CsPbBr_3$ NPLs. As our simulations illustrate it, the regime of nano-platelets growth is achieved in a relatively narrow range of the ligand-ligand interaction energies. For fine-tuning these interaction energies, we used a mixture of ligands in solution (see details in Section 1 of Supporting Information). By fine-tuning the ligand composition, it is possible to achieve the effective ligand-ligand interaction energy required for efficient NPLs growth. As a result, we managed to generate NPLs, which produce *effective* blue emission in the region ~ 460–467 nm.

Results and Discussion

The underlying mechanism of NPLs growth is based on the following theoretical model. Consider a solution containing precursors (atoms) for crystal growth, small nucleated seed crystals, and molecular ligands binding atoms on the crystals' surfaces. We assume that the crystals grow layer by layer with each new atomic layer growing from some nucleus or critical cluster of atoms on the crystal surface. It implies that the slowest event in the growth process is the formation of the critical atomic cluster known as the critical nucleus. The rate of this nucleation process is determined by the critical nucleus' size (number of atoms in the critical cluster) N_{CA} and the nucleation barrier Δ_{CA}. This nucleation barrier characterises the free energy penalty for transferring atoms from solution to the cluster on the crystal surface. Molecular ligands present in the solution can also form a cluster on the crystal surface, which, if this cluster grows over the critical size, can create a compact layer over the entire crystal

facet and block any subsequent growth on it. The process of ligand cluster nucleation is also characterised by the corresponding critical nucleus size N_{CL} and the nucleation barrier Δ_{CL}.

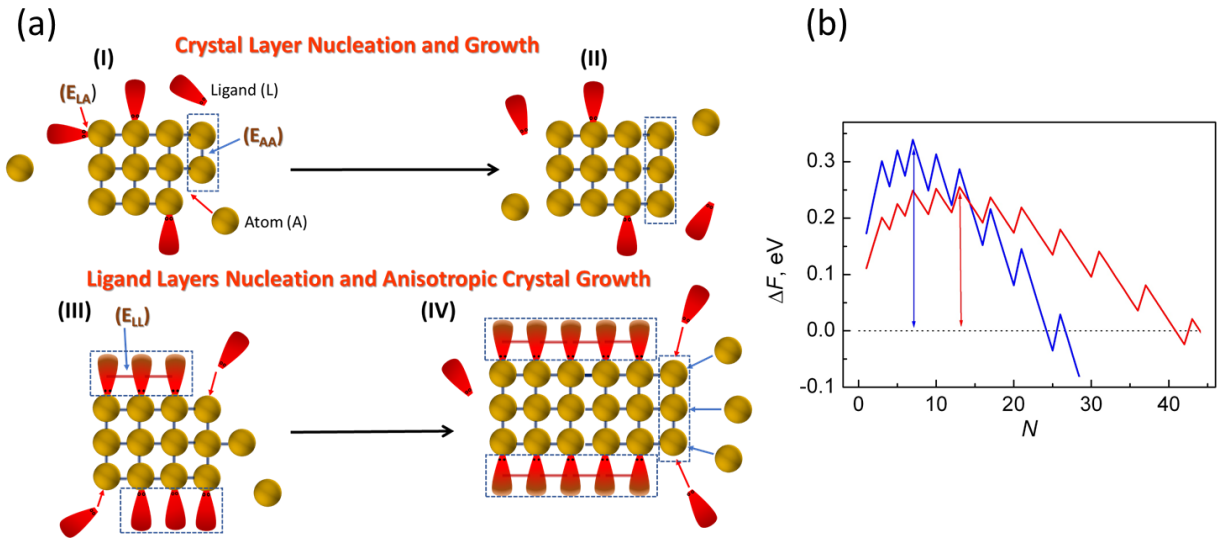

Figure 1. a) Nucleation (panel (I)) and growth (panel (II)) of a new layer of atoms (spheres outlined with dashed lines) on the crystal side. Molecular ligands (cones) cannot nucleate the critical cluster on the short crystal side of 3 atoms (panel (I)), but can do it on the longer side of 4 atoms – see panel (III), which shows two nucleated layers of ligands (cones outlined with dashed lines). Molecular ligands block crystal growth in the vertical direction, leaving the crystal with the ligand layers grow horizontally (panel (IV)). b) Free energy ΔF of the surface cluster (nucleus) calculated on a square lattice of the size 7x7 unit cells as a function of the constituent number N of atoms (blue) or ligands (red) for $k_BT = 34\,meV$ (122 °C), $\varepsilon_{AA} = 109\,meV$ $\varepsilon_{LL} = 66\,meV$, $\varepsilon_{LA} = 171\,meV$ and $n_A = n_L = 2.5\cdot10^{-4}$. The arrows in b) show nucleation barriers Δ_{CA} and Δ_{CL} and indicate corresponding sizes of critical nuclei N_{CL} and N_{CL} for crystal atoms and molecular ligands, respectively.

Both the nucleation barrier and critical nucleus size can be determined by plotting the nucleus' excess free energy $\Delta F_{A(L)}(N)$ versus the number N of constituent atoms/ligands:

$$\Delta F_A(N) = E_A(\varepsilon_{AA}, N) - Nk_BT\ln(n_A),\ \Delta F_L(N) = E_L(\varepsilon_{LL}, \varepsilon_{LA}, N) - Nk_BT\ln(n_L), \quad (1)$$

where $E_A(\varepsilon_{AA}, N)$ and $E_L(\varepsilon_{LL}, \varepsilon_{LA}, N)$ are the total interaction energies of atomic and ligand cluster on the crystal surface, respectively, ε_{AA}, ε_{LL} and ε_{LA} are the pair-wise atom-atom, ligand-ligand, and ligand-atom interaction energies measured relative to atom and ligand

energies in solution, n_A and n_L are the volume fractions of corresponding bare (unbound) species in solution and k_BT is the temperature in energy units. The interaction energies $E_A(\varepsilon_{AA}, N)$ and $E_L(\varepsilon_{LL}, \varepsilon_{LA}, N)$ are the sums of the pair-wise interaction energies assuming that the atoms/ligands in the nuclei occupy the cells in a square lattice and interact only with a maximum of four nearest neighbours in the plane and one neighbour beneath it. The minimum energy configuration of a nucleus on a square lattice is either a square for a wide enough facet or a rectangle otherwise (see Figure S1 in Supporting Information for details). Figure 1a illustrates the mechanism of nucleation and growth of NPLs, while Figure 1b shows the typical shape of the functions $\Delta F_A(N)$ and $\Delta F_L(N)$. The latter curves have serrated shape due to fluctuations in the number of nearest neighbours for each subsequent atom/ligand added during the nucleus formation. Figure 1b presents the most interesting case when the ligands form the critical nucleus much quicker than the atoms due to the lower nucleation barrier $\Delta_{CL} < \Delta_{CA}$ (indicated by the red arrow) despite the fact that the critical size of the ligand nucleus is bigger than that for atoms, namely $N_{CL} > N_{CA}$ (shown by the arrows' position). The ratio of the classical nucleation rates for the atoms (W_A) and ligands (W_L) is estimated for the parameters presented in the caption to Figure 1 as $W_A / W_L \approx 0.1$. Due to the smaller critical nucleus size, the atoms can nucleate new layers on rather small facets where the ligand's critical nucleus cannot be formed at all, as illustrated in Figure 2a. The tiny crystals can, therefore, grow until some of their facets become large enough to accommodate the ligands critical nucleus, as illustrated in Figure 2c. Once this happens, the corresponding facet is quickly covered with ligands which then block any further growth on it. However, the narrower facets which are less likely to be covered with ligands continue supporting the growth process (see Figure 2b). The most likely outcome, in this case, is the growth of narrow-facets crystals, or NPLs.

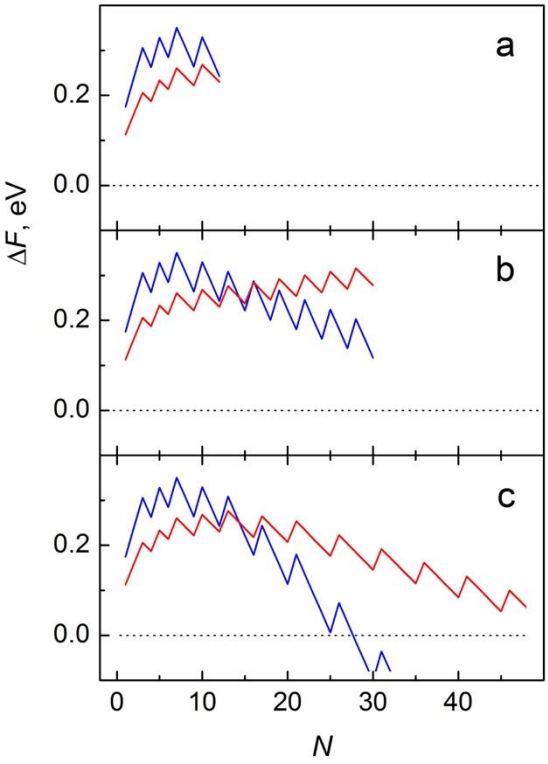

Figure 2. Free energy ΔF of nucleated surface clusters versus the number N of constituent atoms (blue) and ligands (red) on rectangular crystal faces made of a) 3x4 a_0^2 (a_0 is the unit cell length), b) 3x10 a_0^2, and c) 5x10 a_0^2 (for other parameters see the caption for Figure 1). Energy curve for atoms in a) has its maximum at N=7 indicating that if it is passed then the further growth is favourable. In contrast, ΔF for ligands keeps rising meaning that any nucleus will eventually dissolve. A similar picture is shown in b) for a longer face of the same width. In a wider face c) both atomic and ligand nuclei can grow further decreasing their energy.

Kinetic Monte Carlo Simulations

The predictions of our model have been verified numerically using kinetic Monte Carlo (KMC) method to simulate the growth process of an ensemble of 3000 crystals of tetragonal shape. Each crystal facet is assigned two reaction rates, one for the formation of a new atomic layer, and the other one for the creation of a compact layer of ligands. These reaction rates are taken proportional to the classical nucleation rates of the corresponding critical nuclei

$$P_A = K_A \cdot \exp\left(-\frac{\Delta_{CA}}{k_B T}\right),\ P_L = K_L \cdot \exp\left(-\frac{\Delta_{CL}}{k_B T}\right). \qquad (2)$$

Here the Zel' dovich factors, $K_A = 1 - \exp\left(-\frac{\Delta_{AA}}{k_B T}\right)$ and $K_L = 1 - \exp\left(-\frac{\Delta_{LL}}{k_B T}\right)$, are proportional to the probabilities for the corresponding critical cluster to grow and spread over the corresponding crystal facet. The energy factor $\Delta_{AA(LL)}$ represents the difference in the free energy given by Eq. (1) of the complete atomic (ligand) layer ($N = N_{facet}$) and that of the corresponding critical cluster ($N = N_{crit}$). At each time step, a single reaction is randomly chosen according to its relative rate, and the corresponding facet is covered with an extra layer of atoms, or with a layer of ligands. In the former case, the four adjacent facets increase their size, and their reaction rates are updated accordingly. In the case of ligand's layer, the chosen facet becomes inactive, and the corresponding reaction rates are set to zero. Initial volume fractions $n_A = n_L = 2.5 \cdot 10^{-4}$ are decreased at every step according to the numbers of deposited atoms/ligands (see Figure S2 in Supporting Information) illustrating the role of n_A.

To characterise the average crystal shape qualitatively in the ensemble of crystals we introduce distributions of the short, medium, and long edges for constituent crystals with the following interpretation: If all three distributions are grouped close to each other, the crystals' shapes are close to cubic. If the short edges distribution is placed around low values while the other two are centred around large values, the crystals have plate-like shape. If two of the distributions are centred at low values, and the third one is at large values, the crystals are rod-like.

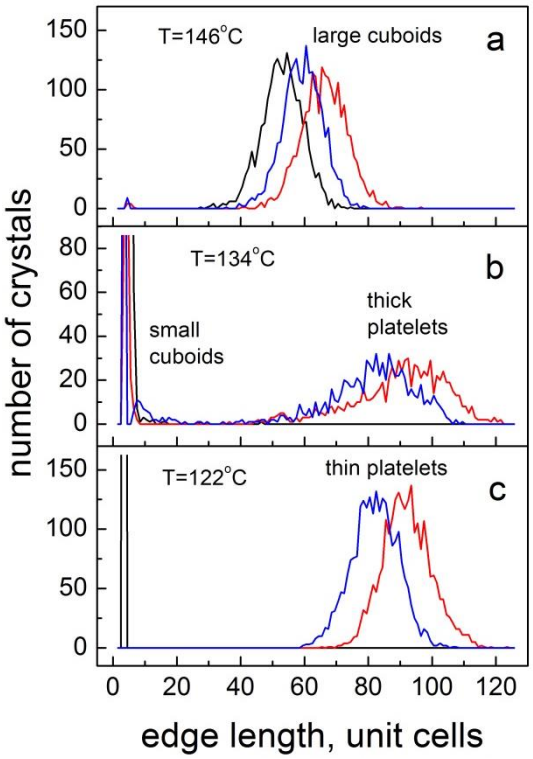

177

178 Figure 3. Distributions of short (black), medium (blue) and long (red) crystal edges in an
179 ensemble of 3000 crystals at different temperatures for the initial concentrations of atoms and
180 ligands in solution $n_A = n_L = 2.5 \cdot 10^{-4}$. All other energy parameters are the same as in the
181 caption to Figure 1. a) crystals are large and have close to cubic shape (large cuboids), b) a
182 mixture of small cuboids (the edges are 6–10 a_0) and relatively thick (6–8 a_0) platelets with a
183 rather broad distribution of lateral sizes, c) thin (~4 a_0) platelets with a narrow distribution of
184 lateral sizes (see also Figure S3 in the Supporting Information).

185

186 Initially, all 3000 crystals are identical cubes of 3x3x3 a_0^3 (a_0 is unit cell length) volume;
187 hence, all crystal facets have identical pairs of atom-related and ligand-related reaction rates.
188 After about a million simulation steps, the shape of crystals changes, as shown in Figure 3, in
189 terms of the edge distributions. According to Figure 3a, at the higher temperatures (146° C),
190 the crystals' shape is close to cubic, as the ligands do not nucleate critical clusters at this
191 temperature; therefore, they cannot affect spontaneous growth of cubic crystals. With a
192 decrease in temperature (see Figures 3b and 3c), the positive entropic contribution to the
193 nucleation barrier and critical nucleus size both decrease and ligands become able to nucleate
194 and produce blocking layers on synthesis facets thus changing the shapes of the crystals.

195 According to Figure 3b, at T=134° C there is a mixture of crystals; some have the shape close
196 to cubic (cuboids) with edge sizes 6–10 a_0 while the others are platelet-like with the thickness
197 around 8–10 a_0 and the length of 60–110 a_0. A further decrease in temperature down to T=122°
198 C (Figure 3c) results in the growth of just thin (~4 a_0) platelets.

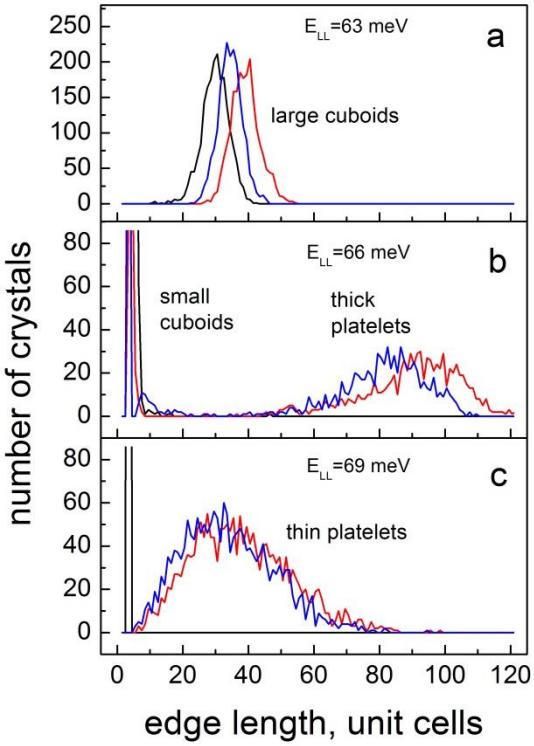

199

200 Figure 4. Distributions of short (black), medium (blue) and long (red) crystal edges in an
201 ensemble of 3000 crystals for $\varepsilon_{AA} = 109\,meV$, $\varepsilon_{LA} = 171\,meV$, $n_A = n_L = 2.5 \cdot 10^{-4}$, $T = 134^o\,C$
202 and different values of ε_{LL}. a) $\varepsilon_{LL} = 63\,meV$, crystals grow as cuboids (see text for
203 explanation), b) $\varepsilon_{LL} = 66\,meV$, this is the same as the curves in Figure 3b, a mixture of small
204 (6-10 a_0) cuboids and thick (6-10 a_0) platelets, c) $\varepsilon_{LL} = 69\,meV$, crystals grow as thin (~4 a_0
205) platelets with very broad lateral size distribution.

206 In simulations, we can also easily vary the ligand-ligand interaction energy ε_{LL}, to study
207 how the ligand choice affects the crystal shape. Experimentally, this energy can be tuned by
208 varying the length of chain-like molecular ligands: the longer the chain, the higher ε_{LL}. Note,
209 that the value of ε_{LA} can be still kept the same if the atomic group binding the surface remains

unchanged. As shown in Figure 4, the effect of increasing ε_{LL} is similar to that of decreasing the temperature. In particular, for $\varepsilon_{LL} = 63 meV$ (Figure 4a), the edge length distributions are very similar to those shown in Figure 3a (the difference in peak positions is due to different growth time). The distributions shown in Figure 4b for $\varepsilon_{LL} = 66 meV$ are the same as in Figure 3b and are presented for comparison. The distributions for $\varepsilon_{LL} = 69 meV$ in Figure 4c like those in Figure 3c show thin (~$4 a_0$) platelets, but the platelets' lateral sizes vary significantly more than those in Figure 3c. This could be due to a very low probability of new atomic layer formation for small crystals (see Supporting Information for details). Any further increase in ε_{LL} results in a significant decrease in ligands layer nucleation barrier, therefore, all the seed crystals' facets become covered with ligands straight away, thus inhibiting any further growth (see Figures S5 and S6 in Supporting Information).

The rationale behind the nucleation-controlled crystal growth mechanism can be understood as follows. The conditions for wide crystal facets to be covered with ligands leaving the narrow facets uncovered are i) a relatively broad distribution of facet widths (crystal edge sizes), and ii) a low enough crystal growth rate. Both these conditions can be met if the growth process is nucleation controlled. Indeed, such growth is characterised by a relatively low probability of layer formation; hence it allows for significant fluctuations in the facet sizes (see Supporting Information). Simultaneously it also means a moderate growth rate giving ligands enough time to form compact layers on broader facets. If the two broader parallel facets are covered with ligands, then the crystal grows as an NPL. If the broader facets are perpendicular to each other, then we would expect the growth of nanorods. The latter regime has also been found in our KMC simulations (see Figure S7 in the Supporting Information). By increasing the temperature or decreasing the ligand-ligand interaction energy ε_{LL}, the probability for a

ligand to nucleate and form a compact layer can be significantly reduced, even down to zero. This decrease results in the growth of bulk crystals rather than platelets (Figures 3a and 4a).

Based on the obtained KMC simulation results, we can identify two main trends taking place upon variation of such system parameters as i) temperature (Figure 3) and ii) ligand-ligand interaction energy (Figure 4). We found that with decreasing temperature, the growing crystals' shape changes from cuboids to platelets. A similar effect takes place when we gradually increase ligand-ligand interaction energy. Both effects were observed experimentally on an example of $CsPbBr_3$ crystals using the three-precursors synthetic approach.

Experimental verification

To characterise the shape of synthesised nanoparticles (see details below and in Supporting Information), the nanoparticles' crystal structure has been characterised using scanning transmission electron micrograph (STEM) analysis. Photoactive perovskites are generally beam-sensitive,[53, 54] and under electron beam exposure the lead (Pb) atoms can segregate out of the $CsPbBr_3$ crystal structure.[55] However, since we are interested in crystal shape rather than high-resolution imaging, the Pb segregation had little effect on the particle size distribution. We also optimised the STEM imaging parameters to avoid the structure damage by the electron beam while keeping the required image resolution (see Supporting Information for details). We examine the optical properties of the synthesised nanoparticles using UV–vis spectroscopy and steady-state PL measurements.

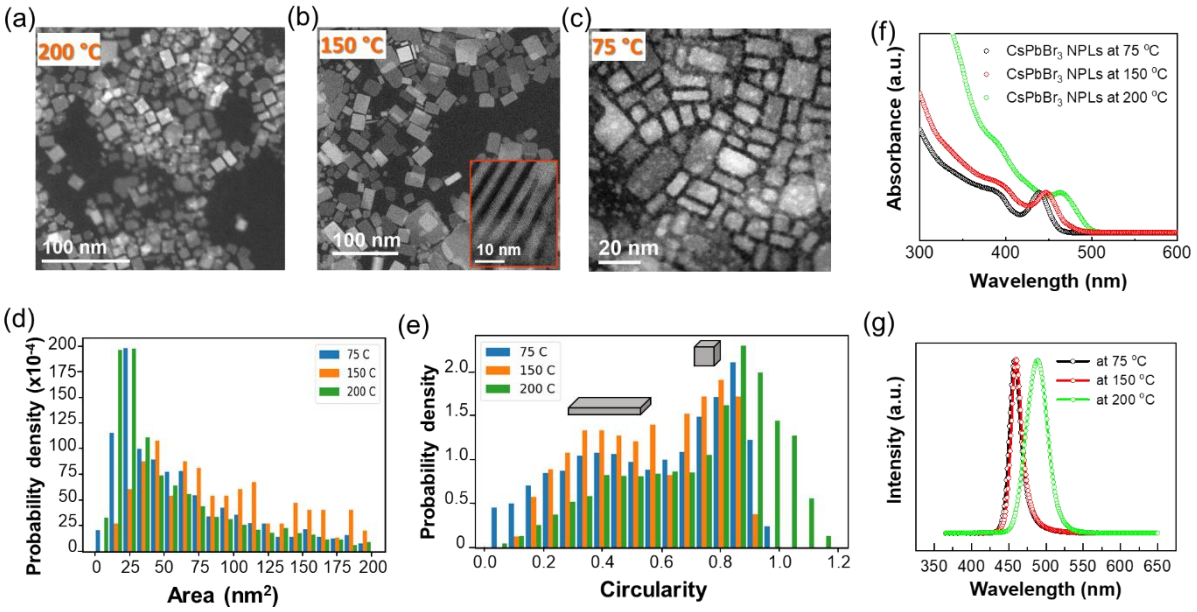

Figure 5. **Influence of reaction temperature on the optical and structural properties of caesium lead tribromide perovskite ($CsPbBr_3$) nanocrystals grown in the presence of oleic acid.** (a) (a–c) Low-magnification scanning transmission electron (STEM) images for $CsPbBr_3$ NCs synthesised from three-precursor approach: (a) at 200 °C giving cuboid crystals, (b) at 150 °C giving quasi-NPLs (reaction time ~10 seconds); inset: high-resolution electron microscopy (HRTEM) where NPLs prepared at 150 °C stack face-to-face or edge-on with the lateral size of (10–15nm), and the thickness of ≥3 nm), and (c) at 75 °C show platelets with lateral size (5–10nm). (d) Normalised histogram of the particle size distribution for the three conditions (T=200, 150, and 75 °C). (e) Normalised histogram of the particle circularity (see text for definition) for the three conditions (T=200, 150, and 75 °C) (f) Normalised absorption spectra of as-prepared pristine $CsPbBr_3$ NPLs (unwashed) in toluene where the NCs are exhibiting a quantum confinement effect. (g) Their normalised steady-state photoluminescence (PL) spectra.

Testing the Temperature Effect. The impact of reaction temperature on the shape of $CsPbBr_3$ nanocrystals has been studied in the range of 75–200 °C while keeping the ratio of oleic acid (1.5 mL)/oleylamine (1 mL) constant. Panels (a) through (c) in Figure 5 show representative STEM-HAADF images of the three samples prepared at 200, 150, and 75 °C, respectively. As these images depict the particles in projection, we need to perform further analysis to better characterise their three-dimensional shape. We used ParticleSpy python package[56] (which wraps Scikit-image[57] and Hyperspy[58] for image analysis and segmentation) and measured the total of 2635, 272, and 1524 particles from 200, 150 and 75 °C samples, respectively. We measured two parameters- presented as histograms in panels (d) and (e): (i) area of the detected

particles and (ii) their circularity, defined as $f_{circularity} = \frac{4\pi A}{P^2}$, where A is the particle's area, and P is the particle's perimeter. We find from the area histogram (panel d) that the peak frequency in area of the particles for 75 and 200 °C case is close to 25 nm^2, whereas for 150 °C case it seems to be slightly lower than 50 nm^2. The circularity parameter, assuming the particles are distributed close to randomly onto the carbon grid support, allows us to make a distinction between the square cuboid and the rectangular cuboid. The inset of panel (b) shows that we routinely encounter particles that have landed on their narrow sides, but there well may be a tendency for them to land on the support with their broad face. Thus, making a distinction between the square cuboid and NPLs (rectangular cuboid) can be drawn indirectly from the circularity plot. The circularity of a perfect circle is 1.0, the circularity of an ideal square is 0.78 while the circularity of a rectangle with a side length of (a x 3a) is 0.59 and of a rectangle with a side length of (a x 5a) is 0.44. Accordingly, in the case of rectangular cuboids, when their narrow face being projected, it would contribute to the peaks around 0.4-0.5 range in the circularity plot. In contrast, the perfectly square cuboid would show a singular peak at 0.78. We expect to see two peaks in the circularity histogram even in the case of pure NPLs; where a fraction of NPLs showing their widest face would look like square cuboids, while those showing one of the narrow faces would be looking like rectangular cuboids. Based on the above and the circularity histogram in panel (e), we can observe that the 150 C sample shows the strongest frequency of the circularity factors of 0.4 with respect to the 0.78 corresponding to perfect square cuboid shape, followed by the 200 C and 75 C cases.

We characterise the optical properties of the as-synthesised batches. We find that decreasing the temperature from 200 °C down to 150 °C and below results in a significant shift of the PL peak position from 490 nm down to 458–460 nm as illustrated in Figure 5f–g The absorption spectrum exhibits a sharp excitonic peak, which also shifts from 465 nm at T=200 °C, down to 448 nm at 150 °C and to 437 nm at 75 °C. The blue shift of the PL spectrum and the of the excitonic absorption peak are attributed to the strong quantum confinement (in NPLs).[18, 33, 34]

We note that Bekenstein *et al.*,[18] examined the influence of the reaction temperature on the morphology of the $CsPbBr_3$ nanocrystals, and they found a similar temperature dependence on the shape's tunability from cuboids to platelets. However, in their case, the value of maximum temperature that can be reached for NPLs' formation is below 130 °C, i.e. significantly lower than our 150 °C. We believe that the cut-off temperature for producing NPLs is mainly influenced by the content of the reaction mixtures and their concertation.

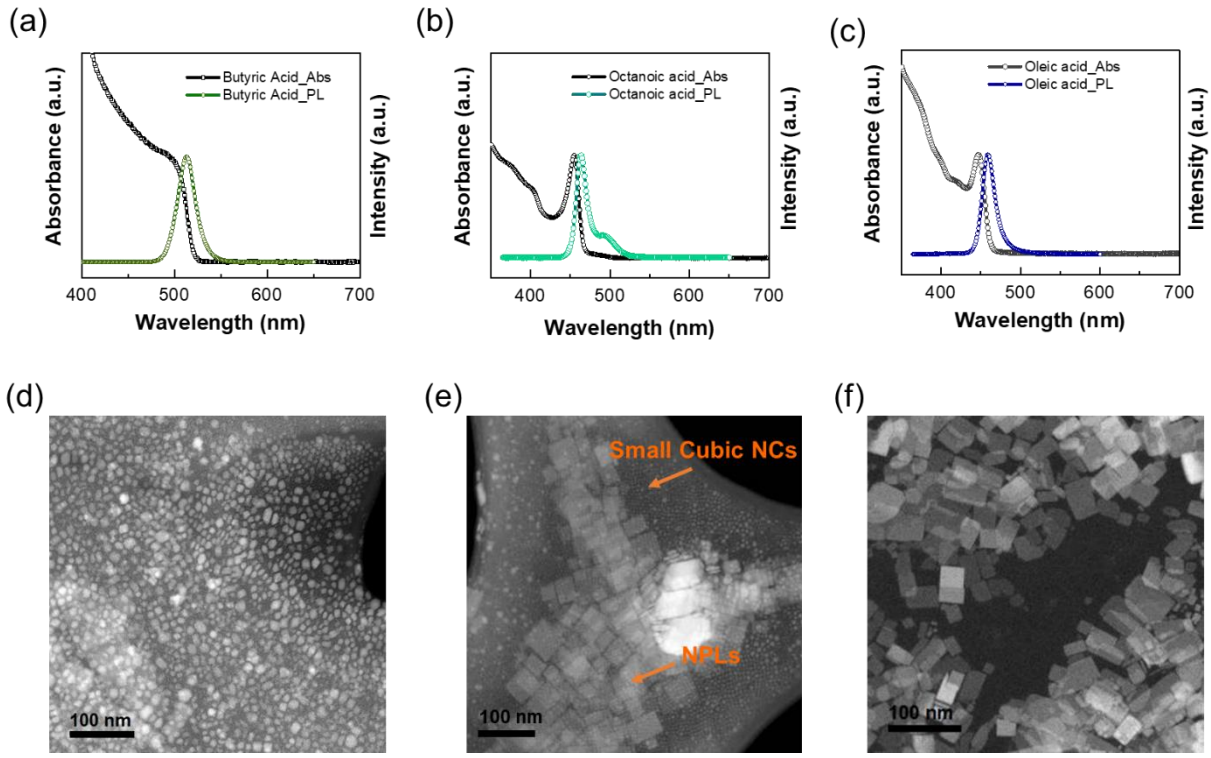

Figure 6. Effect of ligand-ligand interaction on the optical and structural properties of $CsPbBr_3$ nanocrystals grown at 140 °C. (a–c) Normalised absorption and steady-state photoluminescence (PL) spectra of as-prepared pristine $CsPbBr_3$ nanocrystals (unwashed) in toluene in the presence of (a) butyric acid, (b) octanoic acid, and (c) oleic acid. (d–f) The corresponding low-magnification scanning transmission electron (STEM) HAADF images for $CsPbBr_3$ NCs synthesised from a three-precursors approach using acetate salts giving cubic structure in case of butyric acid; (d), mixed cubic/NPLs in case of octanoic acid (e), and (f) NPLs in case of oleic acid where the reaction time is 20 seconds.

Effect of Ligand-ligand interaction energy. To check the influence of ligand-ligand interaction energy ε_{LL}, we carried out the $CsPbBr_3$ crystal growth in the presence of different ligands: butyric acid, octanoic acid, and oleic acid. Recently Manna and co-workers[41] reported the effect of acid/amine ratio on the dimensionality of the $CsPbBr_3$ nanocrystals from cubic to platelets.

They found that the addition of oleylamine in the presence of excess acids which is needed for protonation and formation of oleylammonium, which is essential for the formation of the 2D structures like platelets or rods.[41, 59] In another study, they examined amine-free synthesis of $CsPbBr_3$ nanocrystal, whereby they obtained pure cubic crystals and no any 2D shapes.[60] Therefore, we sought to investigate the influence of the fatty acid chain length on the concentration and solubility of oleylammonium moiety and consequently the growth where we add oleylamine with a fixed concentration in all experiments as the amine source. To characterise the relative strength of ligand-ligand interaction for these acids, we considered their boiling points and used Trouton's rule[61, 62] to relate the former to ligand-ligand interaction energy. According to Trouton's rule, the latter is proportional to average thermal energy at the boiling temperature, namely $\varepsilon_{LL} \approx \frac{3}{2} k_B T_{boil}$, which for the above set of ligands are $T_{boil} = 160^o\,C,\ \varepsilon_{LL} \approx 37\,meV$ – butyric acid, $T_{boil} = 240^o\,C,\ \varepsilon_{LL} \approx 44\,meV$ – octanoic acid, and $T_{boil} = 360^o\,C,\ \varepsilon_{LL} \approx 54\,meV$ – oleic acid.

The obtained values of ε_{LL} most likely give the lowest estimate for the interaction energies between ligands on the crystal surfaces because the ligands on a flat surface are at least partly oriented hence may interact stronger than in the solution. Our experimental results clearly show the shift of the PL peak position towards the blue spectral region from ~512 nm for butyric acid to a very narrow PL (with FWHM = 17 nm) at ~460 nm for oleic acid (see Figures 6a–6c) indicating a decrease in at least one dimension of the crystals, i.e. the thickness of NPLs. We also notice that the PL spectrum for octanoic acid has two peaks, as shown in Figure 6b indicating inhomogeneity of the crystal ensemble from this batch. Figures 6d–6f present the corresponding STEM images of the crystal ensembles for the three synthetic conditions. Panel 6e also illustrates the inhomogeneity of the ensemble of crystals. In the case of butyric acid (Figure 6d), the product is nanocubes and virtually no NPLs are present. We observe NPLs

only in case of using oleic acid as the acid source in the reaction – see Figure 6f. However, we obtain two distinct shapes, small cubic and NPLs, in the same reaction pot by replacing oleic acid by lower carbon chains of octanoic acid. This explains the multiple peaks in the PL of that sample. This observation is consistent with the trend predicted by our KMC simulations, as illustrated in Figure 4. We investigated the surface of the NPLs prepared at 150 C using oleic acid using attenuated total reflection Fourier transform infrared powder spectroscopy (ATR-FTIR) and proton nuclear magnetic resonance (^{1}HNMR), see Figures S11–12. Both FTIR and 1HNMR show the presence of fatty chain ligands (oleic acid, oleylamine and mainly oleylammonium moiety) terminating the surface of the NPLs.

Similarly, Cho *et al.*,[32] observed multiple peaks upon using ligands with the shorter carbon chains in the synthesis of NPLs. We explain the tunability of the particles' morphology as a function of the surface ligand chain length as the following. Increased ligand's chain length results in a stronger ligand-ligand interaction and higher boiling point. Such ligands form the compact layer on the crystal surfaces easier hence can help to generate NPLs at a higher temperature than ligands with shorter chain length in agreement with our KMC simulation results.

Conclusions

The presented simulation and experimental results are consistent with the proposed model of NPLs formation based on competitive nucleation of atoms and ligands on crystal facets. Both modelling and experimental studies found that decreasing the crystal growth temperature or using stronger interacting ligands (the ones with higher boiling temperature) generally helps to obtain crystals in the form of platelets. Development of a more sophisticated theoretical-modelling framework of ligand-controlled crystal growth would be beneficial to improve control over crystal shape and to predict conditions for the formation of rod-like and platelet-

like crystals with a given aspect ratio. Such studies are extremely important for the growing demands of nano-electronics and nano-photonics for sophisticated crystal shapes. Our work also represents a significant advance in the particular problem of synthesis of well-controlled anisotropic $CsPbBr_3$ shapes where the three-precursor approach allows stoichiometry control on the concentration of all elements in the reaction rather than the common use of lead halide (PbX_2) as the only source of anions and cations.

EXPERIMENTAL SECTION:

All procedures were carried on a Schlenk line under oxygen-free conditions and nitrogen gas flow.

Materials. All chemicals were used as received without further purification. Lead acetate trihydrate ($Pb(CH_3COO)_2 \cdot 3H_2O$, 99.99%), caesium carbonate (Cs_2CO_3, reagent Plus, 99%), 1-octadecene (ODE, technical grade, 90%), oleylamine (OLAM, 70%), butyric acid (≥99%), octanoic acid (≥98%), oleic acid (OA, 90%), and HBr acid (48% in water) were purchased from Sigma-Aldrich and used without further purification. All solvents such as toluene, diethyl ether and methyl acetate were anhydrous, and the absolute ethanol were purchased from Sigma-Aldrich.

Preparation of Oleylammonium Bromide Precursor.

The reaction was performed in an ambient condition in fume hood following the procedure reported by Protesescu *et al.*,[51] with modification as following. In a 500 mL flask, oleylamine (OLA, 25 mL), HBr (48% in water, 30 mL), and ethanol (100 mL, absolute >99.8%) were mixed and vigorously stirred for 4 hours at room temperature. Then the content of the flask was evaporated at 40 °C via rotary evaporation to remove all solvents. The obtained product was dissolved back in the minimum amount of absolute ethanol for the re-precipitation process to purify the product from any contamination. The solution was titrated drop by drop of diethyl ether until very few crystals start to precipitate. The flask was moved to the fridge at (–10 °C)

for overnight to complete the re-precipitation of pure white crystals. The white precipitate was then filtrated using Buchner filtration and placed for drying in a vacuum dryer oven at 40 °C for overnight.

Preparation of Caesium Oleate Precursor.

Synthesis of Caesium (Cs)-oleate was done according to literature.[30]

Synthesis of Caesium Lead Tribromide Perovskite Nanoplatelet.

In a typical synthesis of pristine $CsPbBr_3$ NPLs, a 2mmol of lead acetate trihydrate (76 mg) was dissolved in 1.5 mL oleic acid and 1 mL oleylamine in 5 mL of octadecene (ODE) at 120 °C, using the standard air-free technique. A previously prepared and stored under an inert atmosphere, 0.6 mL (0.125 M) of caesium oleate (preheated at 100 °C) was then injected to the solubilised lead precursor and the reaction flask left to continue stirring under vacuum at 120 °C for 1–2 hours. Then, the temperature was increased to 150 °C under the flow of N_2. In a separate vial under N_2, six mmol of oleylammonium bromide (0.21 g) was dissolved in 2 mL of anhydrous toluene and then was swiftly injected into the reaction flask at 145–150 °C. This resulted in changing the colour of the reaction mixture from colourless to transparent light green (chartreuse) colour indicating the formation of the $CsPbBr_3$ NPLs. The growth of the NCs was halted after 10–20 seconds by removing the heat source, and the system was cooled with ice-water bath while simultaneously injecting cold anhydrous toluene into the reaction mixture. The crude solution was collected into a centrifuge tube and was centrifuged for 10 min at 8000 rpm. The supernatant was collected for further use, and any precipitate was discarded.

Washing Process.

For further use or characterisations, these NCs went through a washing process. Typically, we purify the reaction crude solution by precipitating the NPLs with methyl acetate (anti-solvent)

and subsequently re-dissolve in toluene to remove excess unreacted precursors. The toluene colloidal solution is added to methyl acetate in a ratio of 1 to 3. Then this mixture is centrifuged at 8000 rpm for 5 minutes to precipitate the NPs on the sidewall of the centrifuge tube. We then discard the supernatant and re-dissolve the precipitate in toluene. This washing process is repeated twice before further using of the NCs in device fabrication.

Characterisation

Microstructure Characterisation

Aberration-corrected scanning transmission electron microscopy (STEM) was used for atomic resolution characterisation of the as-synthesised NPLs. Samples were deposited on standard lacey carbon grids suspended in toluene (after two cycles of washing by methyl acetate) and left in the air to dry. STEM imaging was performed on an image and probe-corrected JEOL ARM300CF, operated ta 300 kV accelerating voltage. We used a probe current of 2.2 pA for imaging (using a 20 □m probe-forming aperture), providing a probe convergence semi-angle of 16.4 mrad. The annular dark-field signal was acquired at 20 cm camera length, summing the scattered electrons over the range of 36.7 and 200 mrad in semi-angle. This choice of imaging condition, with low beam current (amounting to around 50 e-/Å2 dose per probe position at 2.4 □sec dwell time at 3M magnification) was necessary to minimise the effect of electron induced beam damage.

UV-vis Absorption spectra were recorded using a commercial Varian Cary 60 in a 1 cm cuvette.

Steady-state PL measurement was carried out with an automated spectrofluorometer (Fluorolog, Horiba Jobin-Yvon), with a 450 W Xenon lamp excitation source and a photomultiplier tube detector. The excitation wavelength was 350 nm.

ASSOCIATED CONTENT

Supporting Information

The Supporting Information is available free of charge on the

AUTHOR INFORMATION

Corresponding Authors

*victor.burlakov@maths.ox.ac.uk

ORCID

Victor Burlakov: 0000-0001-5098-1749
Yasser Hassan: 0000-0003-3887-1752
Mohsen Danaie: 0000-0002-9325-7571
Henry J. Snaith: 0000-0001-8511-790X
Alain Goriely:

Notes

The authors declare no competing financial interests.

ACKNOWLEDGEMENT

This work was partially funded by the Engineering and Physical Sciences Research Council (EPSRC) the UK through Grants EP/M005143/1, EP/M015254/2, and EP/R020205/1.

References

1. Stranks, S. D.; Snaith, H. J., Metal-halide perovskites for photovoltaic and light-emitting devices. *Nature Nanotechnology* **2015,** *10*, 391.
2. Tan, Z.-K.; Moghaddam, R. S.; Lai, M. L.; Docampo, P.; Higler, R.; Deschler, F.; Price, M.; Sadhanala, A.; Pazos, L. M.; Credgington, D.; Hanusch, F.; Bein, T.; Snaith, H. J.; Friend, R. H., Bright light-emitting diodes based on organometal halide perovskite. *Nature Nanotechnology* **2014,** *9*, 687.
3. Song, J.; Li, J.; Li, X.; Xu, L.; Dong, Y.; Zeng, H., Quantum Dot Light-Emitting Diodes Based on Inorganic Perovskite Cesium Lead Halides (CsPbX3). *Advanced Materials* **2015,** *27* (44), 7162-7167.
4. Li, G.; Rivarola, F. W. R.; Davis, N. J. L. K.; Bai, S.; Jellicoe, T. C.; de la Peña, F.; Hou, S.; Ducati, C.; Gao, F.; Friend, R. H.; Greenham, N. C.; Tan, Z.-K., Highly Efficient Perovskite Nanocrystal Light-Emitting Diodes Enabled by a Universal Crosslinking Method. *Advanced Materials* **2016,** *28* (18), 3528-3534.
5. Yao, E.-P.; Yang, Z.; Meng, L.; Sun, P.; Dong, S.; Yang, Y.; Yang, Y., High-Brightness Blue and White LEDs based on Inorganic Perovskite Nanocrystals and their Composites. *Advanced Materials* **2017,** *29* (23), 1606859-n/a.
6. Kojima, A.; Teshima, K.; Shirai, Y.; Miyasaka, T., Organometal Halide Perovskites as Visible-Light Sensitisers for Photovoltaic Cells. *Journal of the American Chemical Society* **2009,** *131* (17), 6050-6051.
7. Kim, Y.-H.; Cho, H.; Lee, T.-W., Metal halide perovskite light emitters. *Proceedings of the National Academy of Sciences* **2016,** *113* (42), 11694.
8. Yang, X.; Zhang, X.; Deng, J.; Chu, Z.; Jiang, Q.; Meng, J.; Wang, P.; Zhang, L.; Yin, Z.; You, J., Efficient green light-emitting diodes based on quasi-two-dimensional composition and phase engineered perovskite with surface passivation. *Nature Communications* **2018,** *9* (1), 570.

9. Cho, H.; Kim, J. S.; Wolf, C.; Kim, Y.-H.; Yun, H. J.; Jeong, S.-H.; Sadhanala, A.; Venugopalan, V.; Choi, J. W.; Lee, C.-L.; Friend, R. H.; Lee, T.-W., High-Efficiency Polycrystalline Perovskite Light-Emitting Diodes Based on Mixed Cations. *ACS Nano* **2018,** *12* (3), 2883-2892.
10. Zhang, X.; Sun, C.; Zhang, Y.; Wu, H.; Ji, C.; Chuai, Y.; Wang, P.; Wen, S.; Zhang, C.; Yu, W. W., Bright Perovskite Nanocrystal Films for Efficient Light-Emitting Devices. *The Journal of Physical Chemistry Letters* **2016,** *7* (22), 4602-4610.
11. Chiba, T.; Hayashi, Y.; Ebe, H.; Hoshi, K.; Sato, J.; Sato, S.; Pu, Y.-J.; Ohisa, S.; Kido, J., Anion-exchange red perovskite quantum dots with ammonium iodine salts for highly efficient light-emitting devices. *Nature Photonics* **2018,** *12* (11), 681-687.
12. Xiao, Z.; Zhao, L.; Tran, N. L.; Lin, Y. L.; Silver, S. H.; Kerner, R. A.; Yao, N.; Kahn, A.; Scholes, G. D.; Rand, B. P., Mixed-Halide Perovskites with Stabilized Bandgaps. *Nano Letters* **2017,** *17* (11), 6863-6869.
13. Zou, W.; Li, R.; Zhang, S.; Liu, Y.; Wang, N.; Cao, Y.; Miao, Y.; Xu, M.; Guo, Q.; Di, D.; Zhang, L.; Yi, C.; Gao, F.; Friend, R. H.; Wang, J.; Huang, W., Minimising efficiency roll-off in high-brightness perovskite light-emitting diodes. *Nature Communications* **2018,** *9* (1), 608.
14. Xiao, Z.; Kerner, R. A.; Zhao, L.; Tran, N. L.; Lee, K. M.; Koh, T.-W.; Scholes, G. D.; Rand, B. P., Efficient perovskite light-emitting diodes featuring nanometre-sized crystallites. *Nature Photonics* **2017,** *11* (2), 108-115.
15. Scholes, G. D.; Fleming, G. R., Energy transfer and photosynthetic light harvesting. In *Advances in Chemical Physics*, 2006; Vol. 132, pp 57-129.
16. Congreve, D. N.; Weidman, M. C.; Seitz, M.; Paritmongkol, W.; Dahod, N. S.; Tisdale, W. A., Tunable Light-Emitting Diodes Utilizing Quantum-Confined Layered Perovskite Emitters. *ACS Photonics* **2017,** *4* (3), 476-481.
17. Gong, X.; Voznyy, O.; Jain, A.; Liu, W.; Sabatini, R.; Piontkowski, Z.; Walters, G.; Bappi, G.; Nokhrin, S.; Bushuyev, O.; Yuan, M.; Comin, R.; McCamant, D.; Kelley, S. O.; Sargent, E. H., Electron–phonon interaction in efficient perovskite blue emitters. *Nature Materials* **2018,** *17* (6), 550-556.
18. Bekenstein, Y.; Koscher, B. A.; Eaton, S. W.; Yang, P.; Alivisatos, A. P., Highly Luminescent Colloidal Nanoplates of Perovskite Cesium Lead Halide and Their Oriented Assemblies. *Journal of the American Chemical Society* **2015,** *137* (51), 16008-16011.
19. Shamsi, J.; Dang, Z.; Bianchini, P.; Canale, C.; Di Stasio, F.; Brescia, R.; Prato, M.; Manna, L., Colloidal Synthesis of Quantum Confined Single Crystal CsPbBr3 Nanosheets with Lateral Size Control up to the Micrometer Range. *Journal of the American Chemical Society* **2016,** *138* (23), 7240-7243.
20. Li, J.; Luo, L.; Huang, H.; Ma, C.; Ye, Z.; Zeng, J.; He, H., 2D Behaviors of Excitons in Cesium Lead Halide Perovskite Nanoplatelets. *The Journal of Physical Chemistry Letters* **2017,** *8* (6), 1161-1168.
21. Wu, Y.; Wei, C.; Li, X.; Li, Y.; Qiu, S.; Shen, W.; Cai, B.; Sun, Z.; Yang, D.; Deng, Z.; Zeng, H., In Situ Passivation of PbBr64– Octahedra toward Blue Luminescent CsPbBr3 Nanoplatelets with Near 100% Absolute Quantum Yield. *ACS Energy Letters* **2018**, 2030-2037.
22. Bohn, B. J.; Tong, Y.; Gramlich, M.; Lai, M. L.; Döblinger, M.; Wang, K.; Hoye, R. L. Z.; Müller-Buschbaum, P.; Stranks, S. D.; Urban, A. S.; Polavarapu, L.; Feldmann, J., Boosting Tunable Blue Luminescence of Halide Perovskite Nanoplatelets through Postsynthetic Surface Trap Repair. *Nano Letters* **2018,** *18* (8), 5231-5238.
23. Shamsi, J.; Urban, A. S.; Imran, M.; De Trizio, L.; Manna, L., Metal Halide Perovskite Nanocrystals: Synthesis, Post-Synthesis Modifications, and Their Optical Properties. *Chemical Reviews* **2019,** *119* (5), 3296-3348.
24. Watt, J.; Cheong, S.; Tilley, R. D., How to control the shape of metal nanostructures in organic solution phase synthesis for plasmonics and catalysis. *Nano Today* **2013,** *8* (2), 198-215.
25. Zhang, J.; Hou, C.; Huang, H.; Zhang, L.; Jiang, Z.; Chen, G.; Jia, Y.; Kuang, Q.; Xie, Z.; Zheng, L., Surfactant-Concentration-Dependent Shape Evolution of Au–Pd Alloy Nanocrystals from Rhombic Dodecahedron to Trisoctahedron and Hexoctahedron. **2013,** *9* (4), 538-544.
26. Dong, H.; Wang, Y.; Tao, F.; Wang, L., Electrochemical Fabrication of Shape-Controlled Copper Hierarchical Structures Assisted by Surfactants %J Journal of Nanomaterials. **2012,** *2012*, 6.

27. Xing, R.; Lehmler, H.-J.; L. Knutson, B.; Rankin, S., *Demixed Micelle Morphology Control in Hydrocarbon/Huorocarbon Cationic Surfactant Templating of Mesoporous Silica*. 2010; Vol. 114.
28. Xiao, J.; Qi, L., Surfactant-assisted, shape-controlled synthesis of gold nanocrystals. *Nanoscale* **2011,** *3* (4), 1383-1396.
29. Zhao, N.; Qi, L., Low-Temperature Synthesis of Star-Shaped PbS Nanocrystals in Aqueous Solutions of Mixed Cationic/Anionic Surfactants. **2006,** *18* (3), 359-362.
30. Protesescu, L.; Yakunin, S.; Bodnarchuk, M. I.; Krieg, F.; Caputo, R.; Hendon, C. H.; Yang, R. X.; Walsh, A.; Kovalenko, M. V., Nanocrystals of Cesium Lead Halide Perovskites (CsPbX3, X = Cl, Br, and I): Novel Optoelectronic Materials Showing Bright Emission with Wide Color Gamut. *Nano Letters* **2015,** *15* (6), 3692-3696.
31. Liang, Z.; Zhao, S.; Xu, Z.; Qiao, B.; Song, P.; Gao, D.; Xu, X., Shape-Controlled Synthesis of All-Inorganic CsPbBr3 Perovskite Nanocrystals with Bright Blue Emission. *ACS Applied Materials & Interfaces* **2016,** *8* (42), 28824-28830.
32. Cho, J.; Jin, H.; Sellers, D. G.; Watson, D. F.; Son, D. H.; Banerjee, S., Influence of ligand shell ordering on dimensional confinement of cesium lead bromide (CsPbBr3) perovskite nanoplatelets. *Journal of Materials Chemistry C* **2017,** *5* (34), 8810-8818.
33. Pan, A.; He, B.; Fan, X.; Liu, Z.; Urban, J. J.; Alivisatos, A. P.; He, L.; Liu, Y., Insight into the Ligand-Mediated Synthesis of Colloidal CsPbBr3 Perovskite Nanocrystals: The Role of Organic Acid, Base, and Cesium Precursors. *ACS Nano* **2016,** *10* (8), 7943-7954.
34. Akkerman, Q. A.; Motti, S. G.; Srimath Kandada, A. R.; Mosconi, E.; D'Innocenzo, V.; Bertoni, G.; Marras, S.; Kamino, B. A.; Miranda, L.; De Angelis, F.; Petrozza, A.; Prato, M.; Manna, L., Solution Synthesis Approach to Colloidal Cesium Lead Halide Perovskite Nanoplatelets with Monolayer-Level Thickness Control. *Journal of the American Chemical Society* **2016,** *138* (3), 1010-1016.
35. Yang, D.; Zou, Y.; Li, P.; Liu, Q.; Wu, L.; Hu, H.; Xu, Y.; Sun, B.; Zhang, Q.; Lee, S.-T., Large-scale synthesis of ultrathin cesium lead bromide perovskite nanoplates with precisely tunable dimensions and their application in blue light-emitting diodes. *Nano Energy* **2018,** *47*, 235-242.
36. Sichert, J. A.; Tong, Y.; Mutz, N.; Vollmer, M.; Fischer, S.; Milowska, K. Z.; García Cortadella, R.; Nickel, B.; Cardenas-Daw, C.; Stolarczyk, J. K.; Urban, A. S.; Feldmann, J., Quantum Size Effect in Organometal Halide Perovskite Nanoplatelets. *Nano Letters* **2015,** *15* (10), 6521-6527.
37. Hintermayr, V. A.; Richter, A. F.; Ehrat, F.; Döblinger, M.; Vanderlinden, W.; Sichert, J. A.; Tong, Y.; Polavarapu, L.; Feldmann, J.; Urban, A. S., Tuning the Optical Properties of Perovskite Nanoplatelets through Composition and Thickness by Ligand-Assisted Exfoliation. **2016,** *28* (43), 9478-9485.
38. Weidman, M. C.; Seitz, M.; Stranks, S. D.; Tisdale, W. A., Highly Tunable Colloidal Perovskite Nanoplatelets through Variable Cation, Metal, and Halide Composition. *ACS Nano* **2016,** *10* (8), 7830-7839.
39. Liu, J.; Xue, Y.; Wang, Z.; Xu, Z.-Q.; Zheng, C.; Weber, B.; Song, J.; Wang, Y.; Lu, Y.; Zhang, Y.; Bao, Q., Two-Dimensional CH3NH3PbI3 Perovskite: Synthesis and Optoelectronic Application. *ACS Nano* **2016,** *10* (3), 3536-3542.
40. Dou, L.; Wong, A. B.; Yu, Y.; Lai, M.; Kornienko, N.; Eaton, S. W.; Fu, A.; Bischak, C. G.; Ma, J.; Ding, T.; Ginsberg, N. S.; Wang, L.-W.; Alivisatos, A. P.; Yang, P., Atomically thin two-dimensional organic-inorganic hybrid perovskites. *Science* **2015,** *349* (6255), 1518.
41. Almeida, G.; Goldoni, L.; Akkerman, Q.; Dang, Z.; Khan, A. H.; Marras, S.; Moreels, I.; Manna, L., Role of Acid–Base Equilibria in the Size, Shape, and Phase Control of Cesium Lead Bromide Nanocrystals. *ACS Nano* **2018,** *12* (2), 1704-1711.
42. Green, M. A.; Ho-Baillie, A.; Snaith, H. J., The emergence of perovskite solar cells. *Nature Photonics* **2014,** *8*, 506.
43. Dou, L.; Yang, Y.; You, J.; Hong, Z.; Chang, W.-H.; Li, G.; Yang, Y., Solution-processed hybrid perovskite photodetectors with high detectivity. *Nature Communications* **2014,** *5*, 5404.
44. Xing, G.; Mathews, N.; Lim, S. S.; Yantara, N.; Liu, X.; Sabba, D.; Grätzel, M.; Mhaisalkar, S.; Sum, T. C., Low-temperature solution-processed wavelength-tunable perovskites for lasing. *Nature Materials* **2014,** *13*, 476.

588 45. Imran, M.; Caligiuri, V.; Wang, M.; Goldoni, L.; Prato, M.; Krahne, R.; De Trizio, L.;
589 Manna, L., Benzoyl Halides as Alternative Precursors for the Colloidal Synthesis of Lead-Based Halide
590 Perovskite Nanocrystals. *Journal of the American Chemical Society* **2018,** *140* (7), 2656-2664.
591 46. Ithurria, S.; Dubertret, B., Quasi 2D Colloidal CdSe Platelets with Thicknesses Controlled at
592 the Atomic Level. *Journal of the American Chemical Society* **2008,** *130* (49), 16504-16505.
593 47. Ithurria, S.; Tessier, M. D.; Mahler, B.; Lobo, R. P. S. M.; Dubertret, B.; Efros, A. L.,
594 Colloidal nanoplatelets with two-dimensional electronic structure. *Nature Materials* **2011,** *10* (12), 936-
595 941.
596 48. Riedinger, A.; Ott, F. D.; Mule, A.; Mazzotti, S.; Knüsel, P. N.; Kress, Stephan J. P.; Prins,
597 F.; Erwin, S. C.; Norris, D. J., An intrinsic growth instability in isotropic materials leads to quasi-two-
598 dimensional nanoplatelets. *Nature Materials* **2017,** *16* (7), 743-748.
599 49. Tyagi, P.; Arveson, S. M.; Tisdale, W. A., Colloidal Organohalide Perovskite Nanoplatelets
600 Exhibiting Quantum Confinement. *The Journal of Physical Chemistry Letters* **2015,** *6* (10), 1911-1916.
601 50. Wei, S.; Yang, Y.; Kang, X.; Wang, L.; Huang, L.; Pan, D., Room-temperature and gram-
602 scale synthesis of CsPbX3 (X = Cl, Br, I) perovskite nanocrystals with 50-85% photoluminescence
603 quantum yields. *Chemical Communications* **2016,** *52* (45), 7265-7268.
604 51. Protesescu, L.; Yakunin, S.; Bodnarchuk, M. I.; Bertolotti, F.; Masciocchi, N.; Guagliardi,
605 A.; Kovalenko, M. V., Monodisperse Formamidinium Lead Bromide Nanocrystals with Bright and
606 Stable Green Photoluminescence. *Journal of the American Chemical Society* **2016,** *138* (43), 14202-
607 14205.
608 52. Protesescu, L.; Yakunin, S.; Kumar, S.; Bär, J.; Bertolotti, F.; Masciocchi, N.; Guagliardi,
609 A.; Grotevent, M.; Shorubalko, I.; Bodnarchuk, M. I.; Shih, C.-J.; Kovalenko, M. V., Dismantling
610 the "Red Wall" of Colloidal Perovskites: Highly Luminescent Formamidinium and Formamidinium–
611 Cesium Lead Iodide Nanocrystals. *ACS Nano* **2017,** *11* (3), 3119-3134.
612 53. Rothmann, M. U.; Li, W.; Zhu, Y.; Liu, A.; Ku, Z.; Bach, U.; Etheridge, J.; Cheng, Y.-B.,
613 Structural and Chemical Changes to CH3NH3PbI3 Induced by Electron and Gallium Ion Beams.
614 *Advanced Materials* **2018,** *30* (25), 1800629.
615 54. Rothmann, M. U.; Li, W.; Etheridge, J.; Cheng, Y.-B., Microstructural Characterisations of
616 Perovskite Solar Cells – From Grains to Interfaces: Techniques, Features, and Challenges. *Advanced*
617 *Energy Materials* **2017,** *7* (23), 1700912.
618 55. Dang, Z.; Shamsi, J.; Palazon, F.; Imran, M.; Akkerman, Q. A.; Park, S.; Bertoni, G.; Prato,
619 M.; Brescia, R.; Manna, L., In Situ Transmission Electron Microscopy Study of Electron Beam-
620 Induced Transformations in Colloidal Cesium Lead Halide Perovskite Nanocrystals. *ACS Nano* **2017,**
621 *11* (2), 2124-2132.
622 56. Copyright 2020 to Diamond Light Source Ltd., electron Physical Science Imaging Centre
623 (ePSIC) Harwell Science & Innovation Campus, Didcot, UK; https://epsic-
624 dls.github.io/ParticleSpy/index.html.

625 57. https://scikit-image.org.
626 58. https://hyperspy.org/.
627 59. Almeida, G.; Infante, I.; Manna, L., Resurfacing halide perovskite nanocrystals. *Science* **2019,**
628 *364* (6443), 833-834.
629 60. Almeida, G.; Ashton, O. J.; Goldoni, L.; Maggioni, D.; Petralanda, U.; Mishra, N.;
630 Akkerman, Q. A.; Infante, I.; Snaith, H. J.; Manna, L., The Phosphine Oxide Route toward Lead Halide
631 Perovskite Nanocrystals. *Journal of the American Chemical Society* **2018,** *140* (44), 14878-14886.
632 61. Trouton, F., IV. On molecular latent heat. *The London, Edinburgh, and Dublin Philosophical*
633 *Magazine and Journal of Science* **1884,** *18* (110), 54-57.
634 62. Atkins, P., *Physical Chemistry* Oxford University Press: 1978.

635